Bulletin of the Seismological Society of America, Vol. XX, No. XX, pp. –, – 2018, doi: 10.1785/0120180093

Ⓔ

High-Frequency (> 100 Hz) Earthquakes North of Moloka‘i Detected on the Seafloor at the Aloha Cabled Observatory

by Rhett Butler

Abstract I describe the analysis of 10 earthquakes (M_L 2.7–4.7) that occurred between 2012 and 2017, at depths of 10–33 km, north of Moloka‘i, Hawaiian Islands. Observed on the seafloor Aloha Cabled Observatory (ACO) 24 kHz hydrophone, the events show extraordinary high frequencies up to 165 Hz at distances between 130 and 213 km. The data show a low-frequency spectral decay rate of ω^{-2} that steepens to ω^{-4} beyond 50 Hz. I interpret this change in slope to be the small wavelength manifestation of a smoothly accelerating and decelerating dynamic crack source with larger-scale, variable-rupture velocity. Nearby KIP data from O‘ahu are also considered. Although limited to 45 Hz in bandwidth, comparable spectral slopes are observed. Applying corner frequency analysis to the KIP data, the apparent moments and moment magnitudes of the earthquakes compare well with Hawaiian Volcanos Observatory (HVO) M_L. Characteristic fault dimensions are 0.4–0.9 km, and stress drops $\Delta\sigma$ are 1–9 MPa.

Electronic Supplement: Table of the crustal model used in calculations. Figures comparing the velocity response for the KIP STS-2 and the ACO hydrophone, illustrating the poor *P*- and *S*-wave fits of a single spectral slope from low to high frequency, and detailing *P*- and *S*-wave signal spectra with respect to pre-event background noise.

Introduction

On 9 March 2017, an M_L 4.7 earthquake was recorded in the Hawaiian Islands north of Moloka‘i. The event was well observed on the 24 kHz hydrophone channel at the Aloha Cabled Observatory (ACO) ~100 km north of O‘ahu, where it exhibited frequencies extending greater than 150 Hz at a distance of 160 km, propagating through the oceanic crustal and lithospheric path. Given the relative paucity of high-frequency earthquake data at higher frequencies (20–200 Hz), this event and nine neighboring earthquakes ($2.7 \le M_L \le 4.5$; Fig. 1) were reviewed to determine their characteristic spectral slopes and decay rates, as viewed from the perspective of the earthquake source and propagation path attenuation.

Kinematic and dynamic analysis of the earthquake source have broadly focused upon its spectral characteristics. Eshelby (1957) calculated the analytical solution for a uniform stress drop on a circular source. Haskell (1964) introduced a dislocation model with ω^{-2} fall-off at high frequencies. Based in part upon the assumption of a similarity condition between large and small earthquakes, Aki (1967) introduced, compared, and contrasted two dislocation models with ω^{-2} and ω^{-3} fall-off at high frequencies. Brune (1970) proposed a model of the earthquake source for shear radiation based upon the assumption that faulting occurs instantaneously on a circular crack, its corresponding spectrum falling off at ω^{-2}. Savage (1972) noted from Bracewell (1965) that the high-frequency trend in the source spectrum is defined by the highest-order discontinuity in the signal and is generally proportional to an inverse power of ω. Specifically, "...if the kth derivative of a function becomes impulsive, then the (Fourier) transform behaves as $|\omega|^{-k}$ at infinity." (Bracewell, 1978, p. 144). Hence, the high-frequency spectral fall-off rate is not simply a model parameter but rather a fundamental datum describing the earthquake source and giving insight into the source process.

Dahlen (1974) constructed a 3D kinematic fault in which the rupture initiates or nucleates at a single point and spreads out away from the nucleation to cover the fault surface. The nucleation alone (an impulse in acceleration, or starting phase) dominates the high-frequency radiation, leading to ω^{-3} amplitude spectral decay. The Richards (1973) model also includes an acceleration discontinuity and corresponding ω^{-3} high-frequency spectral decay. Madariaga (1976) analyzed a dynamic model of a circular fault, wherein the spectrum of *P*- and *S*-waves decays like $\omega^{-2.5}$; the additional $\omega^{-1/2}$ decay corresponds to a $\sqrt{t}$ singularity in the source. Madariaga (1977) finds high frequencies are dominantly generated (ω^{-2}) by abrupt changes in rupture velocity. Only starting and stopping phases generate an ω^{-3} spectral

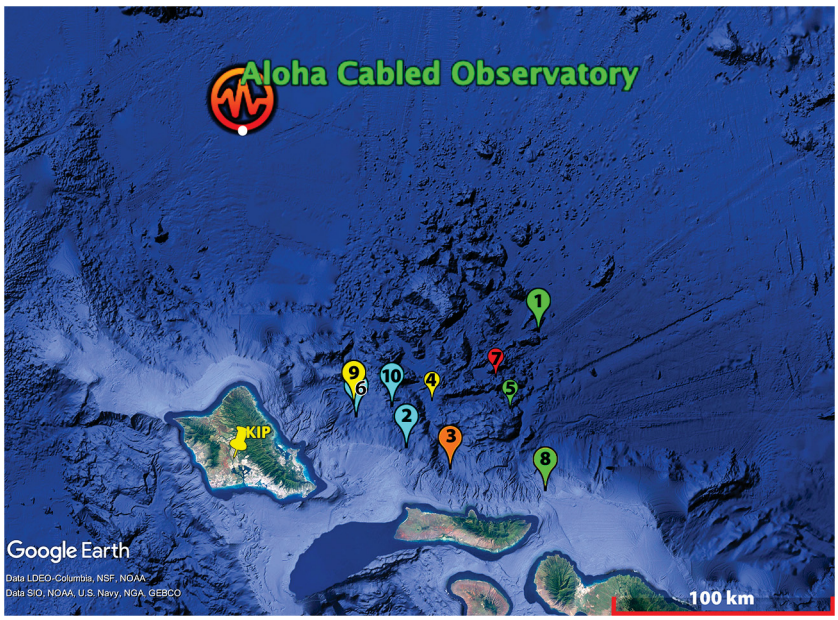

Figure 1. Map of locations of the earthquakes studied herein. The events occur north and northeast of Moloka'i and O'ahu, respectively, centered near 21.6° N, 157.1° W. The Aloha Cabled Observatory (ACO) is on the seafloor at ~4800 m depth, centered at the white dot on the red symbol; KIP, Kipapa, is on O'ahu. The smaller balloon symbols indicate earthquake depths > 30 km. Colors are scaled to earthquake magnitude, in which red is M_L 4.7, orange M_L 4.5, yellow M_L 3.7–3.8, green M_L 3.2–3.5 and cyan M_L 2.7–2.8. Note the 100-km distance scale. Circumstantially, the earthquakes occurred beneath the debris fields of the massive Nu'uanu and Moloka'i landslides, dated to > 0.75 Ma (e.g., Naka *et al.*, 2000).

decay. Kaneko and Shearer (2014, 2015) examined realistic dynamic rupture scenarios for circular and elliptical faults. Following Burridge and Willis (1969) and Dahlen (1974), Kaneko and Shearer (2015) further investigated the directionally anisotropic radiation (frequency and amplitude) from the crack, embedded within the *P* and *S* source radiation from the fault, and noted significant variability with rupture velocity.

The high-frequency spectral decay of the earthquake source is an implicit feature of source models and relates directly to impulsive changes in the earthquake source faulting process. Potentially, observed and measured spectral fall-off rates may form a critical data set characterizing sources. In the 1970s, when strides were made in earthquake source theory, there was little high-frequency data. Nonetheless, there are several studies of note.

Anderson and Hough (1984) assumed an ω^{-2} source spectral decay for the San Fernando earthquake dataset and interpreted additional losses in an ~2–20 Hz band as the effects of Q. Hansen *et al.* (2004) estimated attenuation Q structure of the Kilauea Volcano, Hawaii, from spectra measured to 40 Hz, assuming ω^{-2} spectral decay of the earthquake sources. Shearer *et al.* (2006) stacked source spectra for over 60,000 southern California earthquakes (M_L 1.5–3.5); the averaged stacks were fit to an assumed ω^{-2} model for 2–20 Hz. Zhang *et al.* (2011) measured amplitude spectra of the Cascadia tremor (2.5–20 Hz) with high-frequency spectral decays in the range ω^{-2} and ω^{-3}. Zollo *et al.* (2014) analyzed 717 microearthquakes in Italy in the frequency range 1–40 Hz; the average decay rates for *P*- and *S*-wave were $\omega^{-2.3}$, although one-third of the events showed spectral slopes ≥ 3.

Induced seismicity has exhibited higher frequencies that standard earthquake sources. Abercrombie (1995) noted events ($M_L < 5$) near the Cajon scientific borehole with frequencies up to 100 Hz. Urbancic *et al.* (1996) report observation of 100 Hz to 3 kHz mining-induced microseismic events ($M_L < 0$) recorded at a depth of about 2150 m, with an underground seismic network, with a typical source-sensor distance of 100 m. Both Abercrombie (1995) and Urbancic *et al.* (1996) analyzed their data assuming an ω^{-2} source spectrum and interpreted in terms of path attenuation. Huang *et al.* (2016) report frequencies up to 40 Hz for an induced earthquake sequence in Arkansas.

Consideration of seismic attenuation is an integral part of understanding the high-frequency seismic spectrum. As just noted, many studies have broadly assumed the ω^{-2} source spectrum and interpreted results in terms of frequency-independent Q. In the western Pacific, Butler (1987) simultaneously modeled observed Q_S of Rayleigh waves (100–20 s) and high-frequency (2.5–22.5 Hz) long-range *S*-wave propagation in the oceanic lithosphere (Butler *et al.*, 1987) as a seismic absorption band (Minster, 1978a,b). At low frequencies, Q_S is constant, but at high frequencies (> 5 Hz), Q_S increases as a power law $Q_S \sim f^{1.1}$ with frequency. Chernov (1960) and Wu and Aki (1985) derived elastic wave scattering from small-scale inhomogeneities in the lithosphere as a function of ka, the product of wavenumber and the scale size of inhomogeneities. For $ka \ll 1$ Rayleigh scattering increases as ω^4. For $ka \gg 1$ the scattering increases as ω^2. Both of these forward-scattering effects depend upon the validity of the Born approximation for weak scattering (e.g., Aki and Richards, 1980). Scattering losses increase with frequency, whereas intrinsic losses (Q_S^{-1}) decrease.

Data

The 10 earthquake locations were from the U.S. Geological Survey (USGS) Hawaiian Volcano Observatory (HVO). The events were selected since 2011, when real-time observatory data became available from ACO. The earthquakes are listed in Table 1. The region was limited to that beyond the northern flanks of O'ahu (Nu'uanu) and Moloka'i (Fig. 1), to provide relatively pure oceanic crustal propagation paths to

Table 1
Earthquakes

Map Index	Origin Time, HVO (yyyy/mm/dd hh:mm:ss.s)	M_L	Latitude (°)	Longitude (°)	Depth (km)	km to ACO	km to KIP	Bathymetry (m)
1	2012/02/19 09:18:03.2	3.2	21.94	−156.68	26	163	149	5129
2	2013/04/11 14:27:54.3	2.8	21.47	−157.26	10	161	—	2421
3	2013/06/21 10:04:07.0	4.5	21.38	−157.07	12	180	98	2817
4	2014/05/29 02:40:18.4	3.8	21.66	−157.15	30	149	93	4384
5	2016/06/11 08:14:01.8	3.1	21.63	−156.80	33	175	127	4355
6	2017/01/18 21:15:35.2	2.7	21.59	−157.48	15	139	—	2845
7	***2017/03/09 13:03:39.1***	***4.7***	***21.75***	***−156.87***	***32***	***160***	***124***	***4915***
8	2017/08/23 20:11:21.4	3.5	21.29	−156.65	14	213	—	1100
9	2017/09/12 04:04:40.4	2.8	21.63	−157.32	8	142	—	3177
10	2017/09/16 06:40:37.0	3.7	21.64	−157.49	10	133	60	3052

HVO, Hawaiian Volcanos Observatory; ACO, Aloha Cabled Observatory. Bold italic entry refers to earthquake in Figures 2 and 3.

ACO, because the crustal thickness increases by ~7 km beneath the volcanic core of the islands (Watts and ten Brink, 1989). The depths of events include both shallow (~10 km) and relatively deep earthquakes (~30 km). For shallow events (e.g., earthquake 3 in Table 1), emergent *Pn* is observed leading direct *P* by about 0.25 s. The events in Figure 1 occurred outside of the Hawaii Integrated Seismic Network, and the HVO catalog reports hypocentral errors as < 2 km (horizontal) and < 10 km (in depth). A check of the observed *P* arrival times indicates 8 of the 10 events fit predicted arrivals to $\lesssim$1 s.

Observations of *S* waves at a sea-floor hydrophone are not unusual; many have been reported in marine studies since the early 1980s (e.g., Walker *et al.*, 1983; Butler *et al.*, 1987). However, only the *SV* polarized component is transmitted into the water for a normal, layered structure. Although perhaps not obvious, the *P*- and *S*-wave propagation paths from the events to ACO are entirely contained within the crust and lithosphere and do not include a water path (up to the water reverberation time for *pwP*). To appreciate this, consider the reciprocal path from the ACO sea floor to an event at 10 km depth; there is no *pwP* associated with the destined path to the earthquake hypocenter.

To complement the ACO hydrophone (ALOHA), I also incorporated data from the Global Seismographic Network (GSN) station at KIP, Kipapa on O'ahu. Because the high-frequency (100 Hz) channels were operating in triggered mode, only six of the 10 events were recorded by KIP. The ALOHA hydrophone and KIP STS-2 recordings of the 9 March 2017 earthquake are shown in Figure 2. The ALOHA spectrogram for the event in Figure 3 shows the high-frequency content very clearly above the background noise.

The ACO ALOHA hydrophone data were corrected for instrument response and converted from pressure kPa to particle velocity in m/s, in which $V_P = P/\rho c$ for pressure, density, and sound speed. ACO 24 kHz data were decimated to 400 Hz for ease in processing. For the ACO depth of ~4800 m, the water reverberation time *pwP* is about 6.3 s. Both the *P*- and *S*-wave windows were restricted to 6.1 s following the respective arrivals.

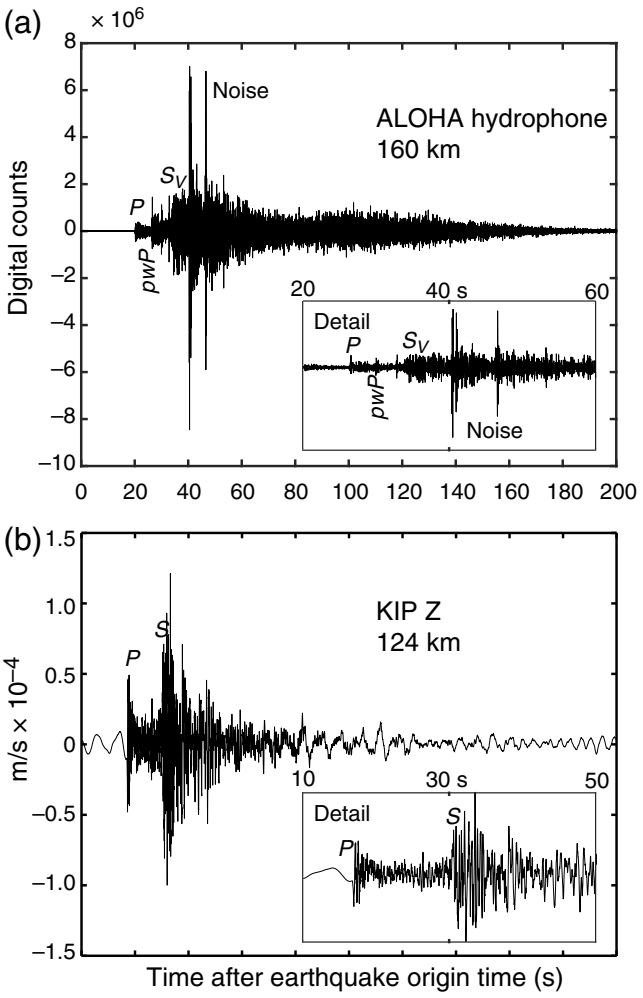

Figure 2. (a) ALOHA hydrophone record (400 samples/s) of M_L 4.7 Moloka'i earthquake of 9 March 2017 (same event as Fig. 3), as recorded by ACO at a distance of 160 km. (b) KIP HHZ record (100 samples/s) at a distance of 124 km. Time is plotted with respect to the earthquake origin time. (Inset) 40 s of detail. Body-wave arrivals—*P*, *S*, *SV*, *pwP*, etc., are evident in the detail inset. Several noise glitches are identified in the ALOHA data that occur outside of the time frame of the study. Note that the first arrival is direct *P* and the higher-frequency content of the ALOHA hydrophone.

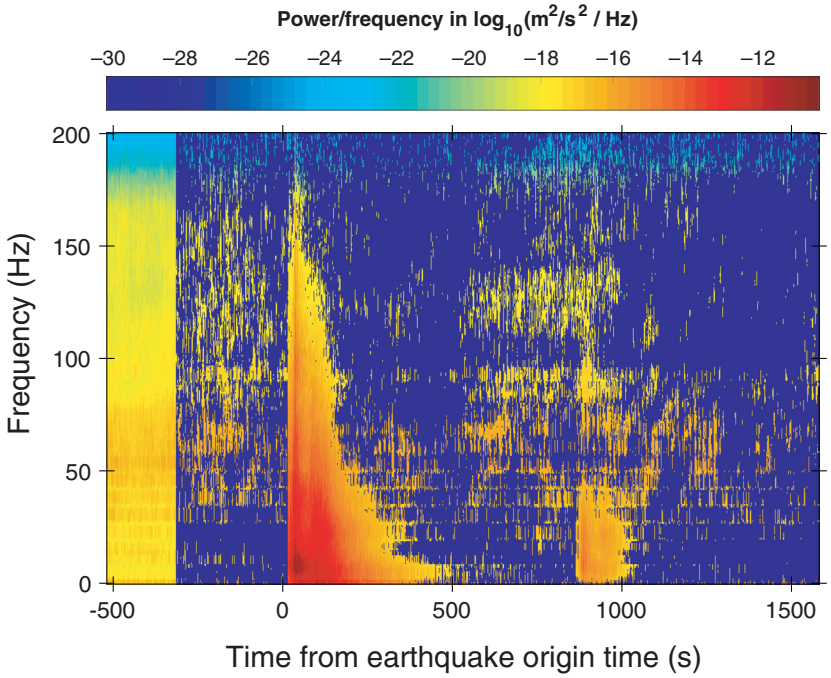

Figure 3. Spectrogram of the M_L 4.7 Moloka'i earthquake of 9 March 2017 (event 7 in Fig. 1), as recorded by ACO at a distance of 160 km, is plotted with respect to the origin time. Frequencies in excess of 150 Hz are observed. Power has been converted to $m^2/s^2/Hz$. The leftmost edge shows the noise power at ~500 s before the event. All data (i.e., noise) with signal-to-noise ratio (SNR) < 2 are then plotted as dark blue (minimum power) to enhance the signal. Note that choosing SNR < 4 gives essentially the same figure.

For KIP, the data were corrected for instrument (STS-2) response (up to a high-frequency limit of 45 Hz). Ⓔ Figure S1 (available in the electronic supplement to this article) compares the velocity responses of the STS-2 and ACO hydrophone. The KIP horizontals were rotated into radial and transverse; though both are considered, I averaged the horizontal results for ease of comparison with prior studies. Given the traditional expression of earthquake spectra in terms of displacement amplitude-second, the velocity data were integrated to displacement in meters. The spectral fall-off rates were calculated by the multitaper method (Park *et al.*, 1987), converting power spectral density to amplitude spectral density. No filtering of the data was applied.

Spectral Analysis

Earthquake spectra for the 10 earthquakes are shown in Figure 4 from the ACO hydrophone. The topmost event (index 7) is the 9 March 2017 earthquake at 160 km distance. *P*- and *S*-data extend to 140 and 163 Hz, respectively, above the background noise (signal-to-noise ratio [SNR] > 2). Above 10 Hz, the hydrophone displacement spectrum decays at $\omega^{-1.8}$ (*P*) and $\omega^{-2.3}$ (*S*). Significantly, this slope changes near 50–60 Hz and then trends at $\omega^{-4.8}$ and $\omega^{-5.5}$, respectively. In both instances, the correlation coefficient r^2 of the linear model exceeds 0.94. Ⓔ Figure S2 shows that a single slope across the whole frequency band does not fit the data.

Consequently, I have fit each *P*- and *S*-wave spectral trend with two slopes. The low- and high-frequency end points are picked above the noise. The first scallop below the peak serves as the low-frequency pick. At highest frequency, the pick is selected with SNR > 2. For a range of midpoints selected, linear models are fit to their respective low–mid and mid–high spectral trends. The quality of fit is determined by sum of the correlation coefficients of both trends; the best fit is defined by the midpoint which maximizes this sum. To balance the influence of high and low frequencies, the linear fits were weighted by $1/f$. Table 2 contains the detailed spectral parameters derived from the ACO hydrophone. Although details differ for the 10 events, the overall impression for Figure 4 is relative congruence among the spectral fall-off rates and transitional frequencies.

In Figure 5, the spectra for the 9 March 2017 earthquake are shown for KIP at 124 km distance. KIP is shown as a reference site with a standard GSN response. However, the paths from the events through the island edifice to KIP differs substantially from those to ACO because of crustal thickening and dipping structures (Watts and ten Brink, 1989), heat flow (e.g., Harris *et al.*, 2000), and association with the mantle plume (Wolfe *et al.*, 2011). Also, KIP's limited high-frequency (< 45 Hz) response cannot detect the slope change seen at ACO at 50–60 Hz. Nonetheless, a transition is still measured in the range 20–30 Hz, with trends at $\omega^{-2.0}$ to $\omega^{-6.0}$ (*P*) and $\omega^{-2.5}$ to $\omega^{-7.5}$ (average of *S* radial and *S* transverse). Whereas both ACO and KIP engender larger spectra rolloff rates at high frequency than observed at low frequency, the observation is more robustly resolved at the ACO hydrophone, given its high-frequency sampling and bandwidth. Until such a time that higher-frequency continuous sampling is incorporated at KIP, the resolution of the rolloff rate is limited to the observation that it increases above 20–30 Hz.

I note that the average low-frequency spectral amplitude ratio *S*/*P* is ~5.1, consistent with seismic velocity factors of α^3 and β^3 in the scalar moment equations, using equations (17) and (18) of Kaneko and Shearer (2015) for M_0^P and M_0^S, respectively. Local crustal-velocity structure (Ⓔ Table S1) is adapted from Watts and ten Brink (1989) and Butler (2003). Table 3 presents the spectral parameters derived from KIP data for all six earthquakes recorded by KIP, including the corner frequencies determined by the intersection of the low-frequency amplitude level with the high-frequency spectral trends.

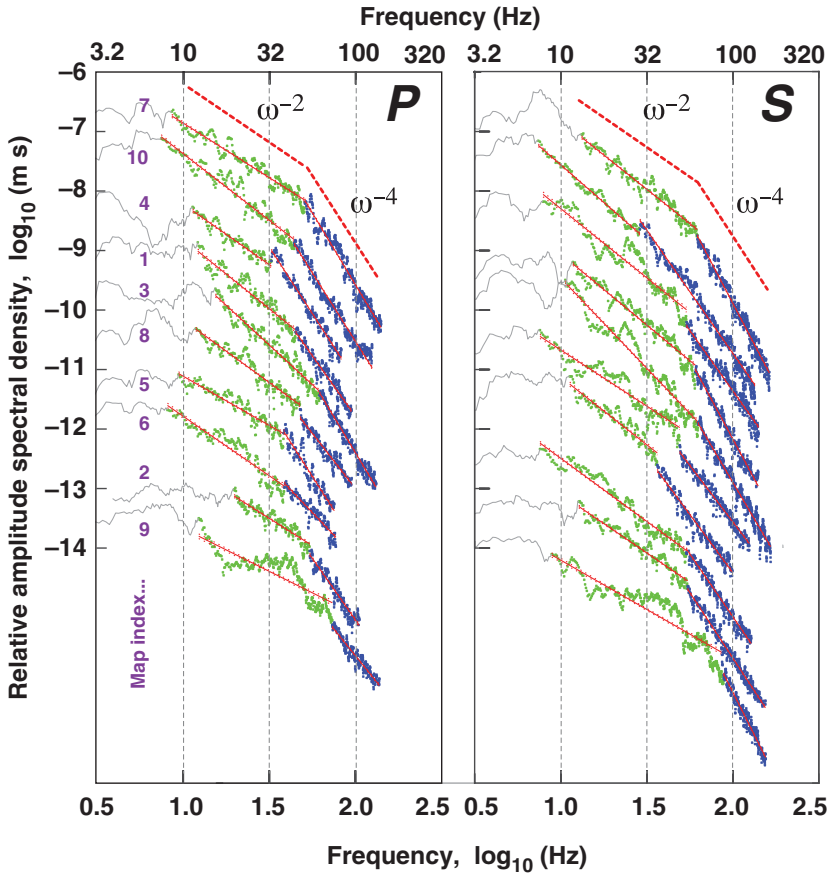

Figure 4. Amplitude spectral density data, as observed at the ACO ALOHA hydrophone for *P*-wave and *S*-wave windows from the 10 earthquakes, are plotted on a log–log scale, with a 200 Hz Nyquist frequency. "Map index" refers to the events in Figure 1 and Table 1. Only data with SNR > 2 are considered. The ordinate scale is relative, because the events have been shifted vertically for clarity. Colored sections show the fit of the data to linear trends (red lines) defining the spectral decay rates $\omega^{-\gamma}$ and corresponding break in slope at frequency ($f_{1\text{–}2}$) in Table 2. Low-frequency (gray) components indicate signals not measured by the colored trends. The red-dotted slopes show the respective ω^{-2} and ω^{-4} power-law relationships for source spectral slopes. Note the unusual spectra for the lowermost event.

Based upon the low-frequency spectral amplitude for the 9 March 2017 event, I calculate the moment magnitudes $M_{\mathrm{w}}^{P} = 4.7$ and $M_{\mathrm{w}}^{S} = 4.6$, both of which compare favorably with the HVO $M_{\mathrm{L}} = 4.7$. These are apparent moments because the average double-couple radiation over the focal sphere is assumed (e.g., Kaneko and Shearer, 2014). Extending the analysis to all six earthquakes observed at KIP, Figure 6 shows a close relationship between HVO M_{L} and KIP M_{w} for *P* and *S*. Similar measures using the ACO hydrophone are vitiated by its inherently limited low-frequency response and the additional analog filtering moderating the microseism peak < 1 Hz.

Having a reasonable match between the apparent moment magnitude and HVO M_{L}, I continue with an analysis of the corner frequency to determine stress drop and a characteristic length of faulting. I have applied the analysis of Kaneko and Shearer (2014), who determined the scaling constants for crack models with symmetric and asymmetric propagation over circular and elliptical cracks. These models form a family of relationships between the corner frequency and the characteristic scale lengths $f_c^{P,S} = \frac{\beta}{l} k^{P,S}$, in which $f_c^{P,S}$ are the *P* and *S* corner frequencies, respectively, l is the fault length scale, β is the shear velocity, and $k^{P,S}$ are scaling constants reflecting the faulting geometry. For example, for the Brune model $k^{S} = 0.37$, whereas the model of Madariaga (1976) has $k^{S} = 0.21$ and $k^{P} = 0.32$. Assuming a rupture velocity of $0.9\,\beta$ for Kaneko

Table 2
P and *S* Spectral Slopes Measured at ACO

Map Index	Earthquake (yyyy/mm/dd)	$P_1\ \omega^{-\gamma}$ (γ)	$f_{1\text{–}2}$ (Hz)	$P_2\ \omega^{-\gamma}$ (γ)	$S_1\ \omega^{-\gamma}$ (γ)	$f_{1\text{–}2}$(Hz)	$S_2\ \omega^{-\gamma}$ (γ)
1	2012/02/19	2.3	45	4.1	2.4	61	5.4
2	2013/04/11	1.8	54	4.1	2.0	55	4.4
3	2013/06/21	2.7	62	4.8	3.0	63	4.9
4	2014/05/29	2.0	32	4.5	2.3	54	4.1
5	2016/06/11	1.7	38	4.5	2.3	36	3.9
6	2017/01/18	2.0	39	3.0	2.1	54	4.2
7	***2017/03/09***	***1.8***	***51***	***4.8***	***2.3***	***62***	***5.5***
8	2017/08/23	2.1	48	3.7	1.9	49	3.8
9	2017/09/12	1.4	73	3.6	1.7	89	5.8
10	2017/09/16	2.2	44	4.6	2.5	29	4.1
	Median	2.0	46	4.3	2.3	54	4.3
	Geomean	2.0	47	4.1	2.2	53	4.6

Bold italic entry refers to earthquake in Figures 2 and 3.

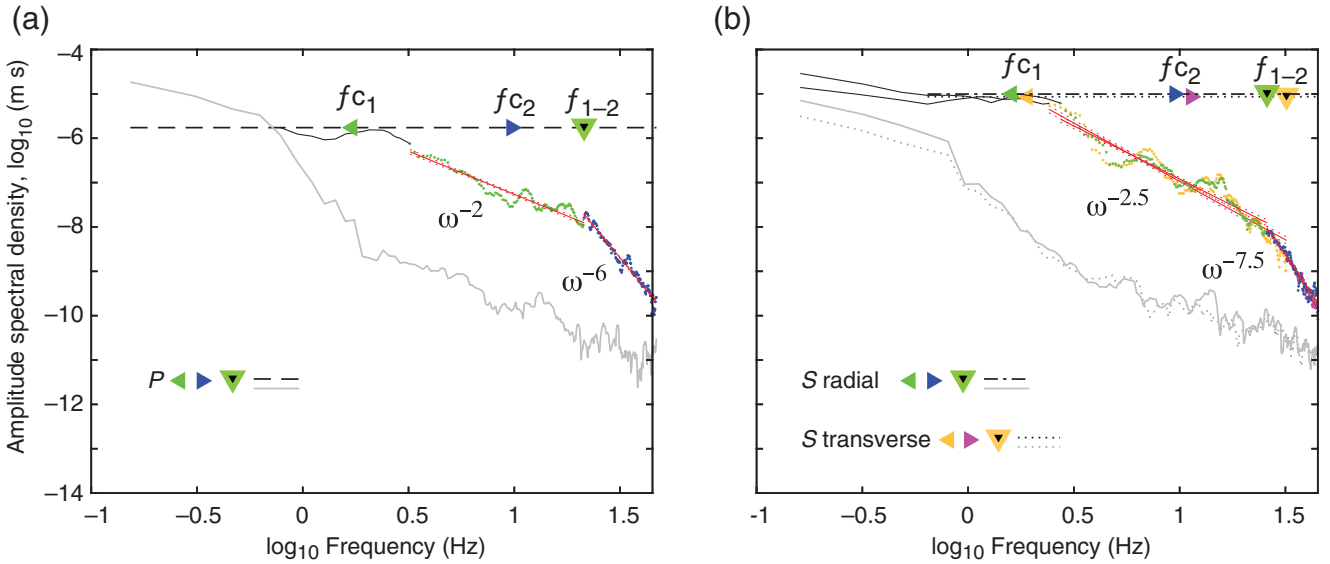

Figure 5. Amplitude spectral density data from KIP for the 9 March 2017 earthquake are plotted on a log–log scale from 0.1 to 45 Hz. *P* waves are shown in (a) and *S* waves in (b), with respective pre-event noise sample. The shear waves were rotated into radial and transverse components and plotted together in separate colors. Spectral slopes (red lines) and their change at high frequency (f_{1-2}) are noted. Red-dotted confidence intervals nearly overlay their respective trends as the coefficients of correlation R^2 ranges from 0.91 to 0.96. Corner frequencies (fc_1 and fc_2) indicate the intersection of these trends with the low-frequency amplitude spectra. Data are summarized in Table 3.

and Shearer (2014), these constants range from $k^P = 0.25$–0.38 and $k^S = 0.26$–0.28. For the 9 March 2017 earthquake, the geometric mean of the four models of Kaneko and Shearer (2014) yields characteristic scale lengths l ($= r$ for circular, and $= \sqrt{ab}$ for elliptical cases) of 0.7 km for *S* and 0.9 km for *P*. For comparison, the Brune model gives $l = 1.1$ km.

For observed high frequencies of ~150 Hz, the corresponding *P*- and *S*-wavelengths are much smaller, ~55 and ~30 m, respectively, than the faulting length scale. Geometrically averaging *P* and *S* measured the stress drop, $\Delta\sigma = 8.5$ MPa. Table 4 summarizes the earthquake faulting characteristics for the six events observed at KIP.

Discussion

I use the earthquake spectral slopes to compare with dynamic crack models of earthquakes to measure the effective singularities in crack propagation for these events in Tables 2 and 3. At both ACO and KIP, the spectral slope at lower frequencies trends as ω^{-2}, but at higher frequencies, the slopes steepen to ω^{-4}. The former is consistent with impulsively varying rupture velocity. An ω^{-3} trend would be consistent with the nucleation models of Dahlen (1974) and Richards (1973), characterized by an impulses in acceleration and deceleration. For ω^{-4}, the process is smoother still, characterized by impulsive jerks ($\dot{a}$), but lacks impulsive acceleration and decelerations or forces. At a higher rate ω^{-5}, the slope corresponds with impulsive "snaps" ($\ddot{a}$).

For the 9 March 2017 earthquake, the characteristic fault length $l \approx 0.9$ km is derived from the corner frequency $f_{c_1} = 1.3$ Hz. The stress drop $\Delta\sigma = 8.5$ MPa. See Table 4 for other earthquakes. The break in slope $f \sim 50$ Hz observed at ACO occurs at *P* and *S* wavelengths $\lambda_P, \lambda_S \ll L$, smaller than the characteristic fault length, in which $\lambda_P = 167$ m,

Table 3

P and *S* Spectral Slopes and Corner Frequencies Measured at KIP

Map Index	Earthquake (yyyy/mm/dd)	Pfc_1 (Hz)	Pfc_2 (Hz)	$P_1\ \omega^{-\gamma}$ (γ)	f_{1-2} (Hz)	$P_2\ \omega^{-\gamma}$ (γ)	Sfc_1 (Hz)	Sfc_2 (Hz)	$S_1\ \omega^{-\gamma}$ (γ)	f_{1-2} (Hz)	$S_2\ \omega^{-\gamma}$ (γ)
1	2012/02/19	3.0	19.6	1.6	33	8.3	2.8	7.8	1.9	23.6	4.3
3	2013/06/21	1.9	10.8	1.7	23	5.4	1.0	3.7	1.9	10.6	3.9
4	2014/05/29	2.2	10.2	2.0	23	4.7	2.7	4.3	2.8	12.4	3.3
5	2016/06/11	3.4	12.0	2.2	21	5.5	2.7	9.2	1.8	17.0	5.0
7	***2017/03/09***	***1.7***	***9.7***	***2.0***	***21***	***5.9***	***1.7***	***10.5***	***2.5***	***28.8***	***7.5***
10	2017/09/16	3.4	15.3	2.4	30	7.2	1.7	6.7	2.3	15.7	5.4
	Median	2.6	11.4	2.0	23.1	5.7	2.2	7.3	2.1	16.4	4.7
	Geomean	2.5	12.5	2.0	24.8	6.1	2.0	6.6	2.2	16.9	4.8

Bold italic entry refers to earthquake in Figures 2 and 3.

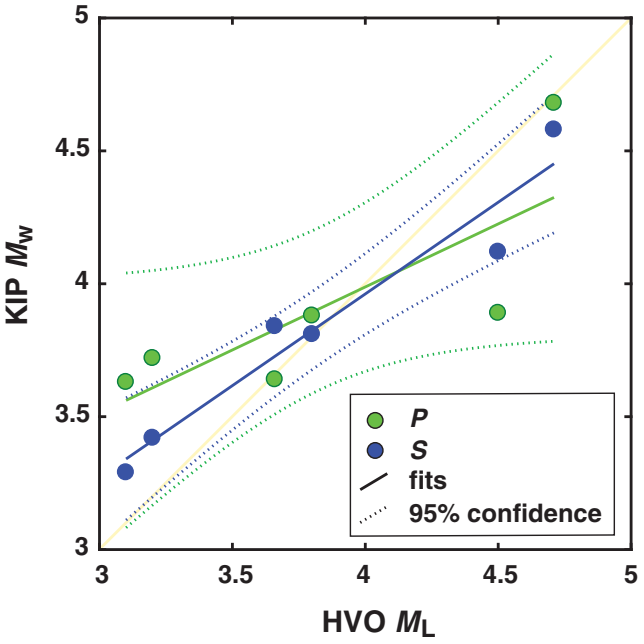

Figure 6. The correlation of magnitude estimates is plotted for *P* and *S* M_w, as observed at KIP versus Hawaiian Volcanos Observatory (HVO) M_L. Linear fits (green and blue lines) and 95% confidence limits (colored dots are for *P* and *S*) are indicated. The *S*-wave trend shows a lower variance and better matches HVO M_L, though both *P* and *S* fit the HVO trend (yellow) within the confidence bounds.

$\lambda_S = 96$ m, $L = 800$ m. Hence, small-scale features of the fault rupture smoothly in acceleration and deceleration. At KIP, this break-in-slope transition is nominally out of band. For KIP, the transition appears at $f \sim 20$ Hz, with wavelengths $\lambda_P = 420$ m and $\lambda_S = 240$ m, both being more substantial fractions of the fault area. Otherwise, given (1) the differing propagation paths (oceanic vs. island) and (2) the orthogonal azimuths from the earthquake to ACO and KIP, there is not a great expectation for ACO and KIP to be the same. Nevertheless, the KIP and ACO data do converge to the same spectral slopes, ω^{-2} and ω^{-4}.

Further progress in high-frequency measurements at KIP will require a higher sampling rate and continuous monitoring. Better still would be to install a cabled seismometer at ACO sampled at ~400 samples/s. The latter would not only clarify the high-frequency observations, but also contribute to routine earthquake monitoring by HVO for offshore coverage.

Kaneko and Shearer (2015) noted significant variation in apparent slope and corner frequency as a function of rupture velocity, azimuth, and colatitude from the fault surface. Although only circumstantial, one of the ten earthquakes (12 September 2017) studied shows significant spectral nonlinearity that may possibly be ascribed to dynamic focusing effects of the crack propagation. This earthquake is event number 10 in Figure 4, characterized by a level spectrum between 17 and 45 Hz for *P* waves and shallow spectral slope of $\omega^{-0.5}$ for *S* waves.

In this article, I have focused upon high-frequency characteristics of the earthquake sources. Of course, the data are also convolved with an intrinsic, frequency-dependent Q (Butler, 1987; Butler *et al.*, 1987) and with a crustal lithosphere scattering operator (Wu and Aki, 1985). These high frequencies are consistent with the development of long-range *Po* and *So* observed in the Pacific, in which 15 Hz shear waves are observed propagating up 3300 km (Walker *et al.*, 1983). Nonetheless, modeling for intrinsic attenuation is vexed with more unknowns than constraints. If losses are restricted to rigidity, then $Q_P = \frac{9}{4} Q_S$. However, Butler *et al.* (1987) observed higher attenuation of *P* than *S* at frequencies > 5 Hz, which may indicate losses in compression. Further, in terms of an absorption-band Q model, Butler (1987) noted that a high-frequency relaxation time, $\tau \approx 0.03 (f \sim 5$ Hz), fit with observed $Q_S \sim f^1$ seen in the western Pacific (Butler, 1987).

The observation of high-frequency *S* waves up to 163 Hz at 162 km distance from the hypocenter of the earthquake source seems extraordinary. To place the possible path Q_S into perspective, the *S* waves travel about 5700 wavelengths. For 3D geometric spreading, the energy decreases as $1/R^2$. Relative to a wavelength λ_S at the earthquake source, this is $(\lambda_S/R)^2 = 3.3 \times 10^{-8}$. The same energy loss is achieved with $\overline{Q}_S \sim 2002$. For 50 Hz *S* waves at the same distance, the equivalent loss requires $\overline{Q}_S \sim 711$. These values are the values of $\overline{Q}_S$ needed to be equivalent to geometric losses but are not a measure of absolute Q_S. Rather, if $Q_S > 2000$, then geometric spreading dominates. However,

Table 4
Earthquake Faulting Characteristics Derived

		Magnitude			Fault *L* (km)		Stress Drop (MPa)	
Map Index	Earthquake	*P* M_w	*S* M_w	HVO M_L	*P*	*S*	*P*	*S*
1	2012/02/19	3.7	3.5	3.2	0.5	0.4	0.9	0.8
3	2013/06/21	3.9	4.2	4.5	0.7	1.1	3.8	0.7
4	2014/05/29	3.9	3.9	3.8	0.7	0.5	1.3	2.6
5	2016/06/11	3.6	3.3	3.1	0.4	0.5	0.8	0.5
7	***2017/03/09***	***4.7***	***4.6***	***4.7***	***0.9***	***0.7***	***7.7***	***10.3***
10	2017/09/16	3.6	3.9	3.7	0.4	0.6	8.0	1.2

Bold italic entry refers to earthquake in Figures 2 and 3

for $Q_S < 2000$, the attenuation losses dominate over geometric spreading energy losses.

Regarding scattering, the high-frequency approximation, $ka \gg 1$, in which $k = 2\pi f/c$, $f = 150$ Hz, $c = 8$ km/s, and $a = 1$ km, yielding $ka = 118 \gg 1$. However, to use the scattering formulas of Wu and Aki (1985), we must also meet the Born approximations (e.g., Aki and Richards, 1980), $\mathcal{B} = 2\langle\mu^2\rangle k^2 aR \ll 1$, in which $\langle\mu^2\rangle$ is the velocity perturbation $(\sim 2\%)^2$ and $R = 160$ km. Calculating this constraint with the parameters noted, $\mathcal{B} = 1777 \not< 1$. In principle, the condition $ka \gg 1$ implies scattering proportional to ω^2 (Wu and Aki, 1985). However, because the Born approximations are not met (the scattered energy must be small compared to the primary wavefield energy), we cannot simply employ the scattering formulas of Wu and Aki (1985).

The effects on the spectral slopes from elastic scattering differ from intrinsic attenuation. If intrinsic Q is constant, then there is not a power law dependence. If $Q_S \sim f^1$ then energy losses decrease with frequency. However, for elastic scattering losses proportional to ω^2, the energy losses increase as the square of frequency. Hence, the shift in slope (Fig. 4) from ω^{-2} to ω^{-4} at about 50 Hz, could indicate additional scattering losses for wavelengths $\lambda_S < 100$ and $\lambda_P < 170$ m.

Summary

I have analyzed ten earthquakes north of Moloka‘i between M_L 2.7 and 4.7 during 2012–2017. The hydrophone data for the earthquakes from the ACO show remarkable high frequencies, up to 140 Hz for *P* waves and 165 Hz for *S* waves, at distances of 133–213 km. These propagation paths are wholly within the solid earth. Spectral slopes derived from the data show two distinct regions: (1) a lower-frequency trend (10– ~ 50 Hz) corresponding to ω^{-2}, and a higher frequency trend (~50–165 Hz) decreasing as ω^{-4}. For comparison, six of the 10 events were also recorded at the nearby KIP station on O‘ahu. Although the KIP bandwidth is limited to 45 Hz, a similar low-frequency spectral slopes of ω^{-2} are observed, with the higher frequency slopes following ω^{-5}. The transitional frequency occurs near 50 Hz for the ACO data set and ~20 Hz for the KIP data set.

The spectral fall-offs (ω^{-2} and ω^{-4}, respectively) are consistent with larger-scale rupture velocity variation, coupled with smooth acceleration and deceleration (jerky motion via impulsive $\dot{a}$) at smaller wavelengths beyond the break in slope. For ω^{-2} spectral slopes, Madariaga (1977, p. 629) states, “When the rupture velocity is constant, … there is practically no high-frequency radiation by the rupture front. On the other hand, strong radiation occurs when the rupture velocity changes abruptly…generating a strong discontinuous wave front. High frequencies are associated with these discontinuities in the radiation.” The higher frequency ω^{-4} spectral slope is consistent with jerking motions but may also be influenced by ω^2 elastic scattering along the propagation path.

Applying corner spectral analysis to the KIP data, the characteristic fault length l is about 800 m for the largest earthquake and ~500 m for the others. At 50 Hz, the wavelengths are about 160 and 90 m for *P* and *S*, respectively, or < 20% of l. Hence, having smooth acceleration and deceleration over smaller fault scales are internally consistent. Similarly, deriving both apparent moments and M_w for KIP, these compare well with HVO local magnitude M_L. Calculating the stress drops $\Delta\sigma$ based upon the low-frequency corner (f_{c_1}), the largest event shows a stress drop of ~9 MPa, with the other events at ~1 MPa.

Using a hydrophone is perhaps unusual for earthquake studies, but the ability to see into the high-frequency (> 100 Hz) earthquake source is refreshing. Although the ACO hydrophone cannot effectively resolve lower-frequency features, by comparison with nearby KIP data, a reasonably coherent picture emerges suggesting that high frequencies not typically observed by land-based seismologists have a steeper spectral slope than ω^{-2} at frequencies beyond 20–50 Hz.

Finally, the successful, close integration of ACO hydrophone and KIP data makes a good case for installing a broad bandwidth seismometer at ACO. Providing for “purely oceanic” paths will lessen the uncertainties and complications of propagation into the O‘ahu island edifice. In principle, the KIP high-frequency sensors should be operated in a continuous (not triggered) mode at 400 Hz sampling. Plans to upgrade the ACO hydrophone with a better sensor calibrated to lower frequencies are welcomed.

Data and Resources

All data were obtained either from the Aloha Cabled Observatory (ACO) or the Incorporated Research Institutions for Seismology (IRIS) Data Management System (KIP). Earthquake locations were obtained from the U.S. Geological Survey/Hawaiian Volcanos Observatory (USGS/HVO) catalog.

Acknowledgments

As the Aloha Cabled Observatory (ACO) begins its second decade as Earth’s deepest seafloor observatory, the author acknowledges and commends the scientific vision of the ACO team and their leadership in creating this extraordinary, real time, cabled facility for deep-ocean science. The author recognizes and thanks Frederick K. Duennebier, in this year of his passing, for his exceptional, lifelong contributions to oceanic seismology. The author thanks the National Science Foundation (NSF) for its support of the ACO under NSF Grant Numbers OCE 1539244 and OCE 1738054 and the U.S. Geological Survey (USGS), IRIS, and the Pacific Tsunami Warning Center for continuing operation of the Global Seismographic Network (GSN) station KIP on O‘ahu. The author thanks anonymous reviewers for their clarifying suggestions. Publication Numbers 10414 (School of Ocean and Earth Science and Technology [SOEST]) and 2353 (Hawai‘i Institute of Geophysics and Planetology [HIGP]).

References

Abercrombie, R. E. (1995). Earthquake source scaling relationships from −1 to 5 M_L using seismograms recorded at 2.5-km depth, *J. Geophys. Res.* **100,** 24,015–24,036.

Aki, K. (1967). Scaling law of seismic spectrum, *J. Geophys. Res.* **72,** no. 4, 1217–1231.

Aki, K., and P. G. Richards (1980). *Quantitative Seismology Theory and Methods*, Vol. I/II, W. H. Freeman, San Francisco, California.

Anderson, J. G., and S. E. Hough (1984). A model for the shape of the Fourier amplitude spectrum of acceleration at high frequencies, *Bull. Seismol. Soc. Am.* **74,** no. 5, 1969–1993.

Bracewell, R. N. (1965). *The Fourier Transform and Its Applications*, Chapter 8, McGraw-Hill, New York, New York, 381 pp.

Bracewell, R. N. (1978). *The Fourier Transform and Its Applications*, Second Ed., Chapter 8, McGraw-Hill, New York, New York, 444 pp.

Brune, J. N. (1970). Tectonic stress and the spectra of seismic shear waves from earthquakes, *J. Geophys. Res.* **75,** no. 26, 4997–5009.

Burridge, R., and J. R. Willis (1969). The self-similar problem of the expanding elliptical crack in an anisotropic solid, in *Mathematical Proceedings of the Cambridge Philosophical Society*, Vol. 66**,** no. 2, Cambridge University Press, Cambridge, United Kingdom, 443–468.

Butler, R. (1987). A seismic absorption band in the western Pacific lithosphere, *Bull. Seismol. Soc. Am.* **77,** no. 1, 266–269.

Butler, R. (2003). The Hawaii-2 observatory: Observation of nanoearthquakes, *Seismol. Res. Lett.* **74,** no. 3, 290–297.

Butler, R., C. S. McCreery, L. N. Frazer, and D. A. Walker (1987). High-frequency seismic attenuation of oceanic *P* and *S* waves in the western Pacific, *J. Geophys. Res.* **92,** no. B2, 1383–1396.

Chernov, L. A. (1960). *Wave Propagation in a Random Medium*, McGraw-Hill, New York, New York, pp. 168.

Dahlen, F. A. (1974). On the ratio of *P*-wave to *S*-wave corner frequencies for shallow earthquake sources, *Bull. Seismol. Soc. Am.* **64,** no. 4, 1159–1180.

Eshelby, J. D. (1957). The determination of the elastic field of an ellipsoidal inclusion, and related problems, *Proc. Math. Phys. Sci.* **241,** no. 1226, 376–396.

Hansen, S., C. Thurber, M. Mandernach, F. Haslinger, and C. Doran (2004). Seismic velocity and attenuation structure of the east rift zone and south flank of Kilauea Volcano, Hawaii, *Bull. Seismol. Soc. Am.* **94,** no. 4, 1430–1440, doi: 10.1785/012003154.

Harris, R. N., R. P. Von Herzen, M. K. McNutt, G. Garven, and K. Jordahl (2000). Submarine hydrogeology of the Hawaiian archipelagic apron: 1. Heat flow patterns north of Oahu and Maro Reef, *J. Geophys. Res.* **105,** no. B9, 21,353–21,369.

Haskell, N. A. (1964). Total energy and energy spectral density of elastic wave radiation from propagating faults, *Bull. Seismol. Soc. Am.* **54,** no. 6A, 1811–1841.

Huang, Y., G. C. Beroza, and W. L. Ellsworth (2016). Stress drop estimates of potentially induced earthquakes in the Guy-Greenbrier sequence, *J. Geophys. Res.* **121,** no. 9, 6597–6607.

Kaneko, Y., and P. M. Shearer (2014). Seismic source spectra and estimated stress drop derived from cohesive-zone models of circular subshear rupture, *Geophys. J. Int.* **197,** no. 2, 1002–1015.

Kaneko, Y., and P. M. Shearer (2015). Variability of seismic source spectra, estimated stress drop, and radiated energy, derived from cohesive-zone models of symmetrical and asymmetrical circular and elliptical ruptures, *J. Geophys. Res.* **120,** no. 2, 1053–1079.

Madariaga, R. (1976). Dynamics of an expanding circular fault, *Bull. Seismol. Soc. Am.* **66,** no. 3, 639–666.

Madariaga, R. (1977). High-frequency radiation from crack (stress drop) models of earthquake faulting, *Geophys. J. Int.* **51,** no. 3, 625–651.

Minster, J. B. (1978a). Transient and impulse responses of a one-dimensional linearly attenuating medium. I. Analytical results, *Geophys. J. Roy. Astron. Soc.* **52,** 479–501.

Minster, J. B. (1978b). Transient and impulse responses of a one-dimensional linearly attenuating medium. II. A parametric study, *Geophys. J. Roy. Astron. Soc.* **52,** 503–524.

Naka, J., E. Takahasi, D. Clague, M. Garcia, T. Hanyu, E. Herrero-Bervera, J. Ishibashi, O. Ishizuka, K. Johnson, T. Kanamatsu, *et al.* (2000). Tectono-magmatic processes investigated at deep-water flanks of Hawaiian volcanoes, *Eos Trans. AGU* **81,** no. 20, 221–226.

Park, J., C. R. Lindberg, and F. L. Vernon (1987). Multitaper spectral analysis of high-frequency seismograms, *J. Geophys. Res.* **92,** no. B12, 12675–12684

Richards, P. G. (1973). The dynamic field of a growing plane elliptical shear crack, *Int. J. Solids Struct.* **9,** no. 7, 843–861.

Savage, J. C. (1972). Relation of corner frequency to fault dimensions, *J. Geophys. Res.* **77,** no. 20, 3788–3795.

Shearer, P. M., G. A. Prieto, and E. Hauksson (2006). Comprehensive analysis of earthquake source spectra in southern California, *J. Geophys. Res.* **111,** no. B6, doi: 10.1029/2005JB003979.

Urbancic, T. I., C.-I. Trifu, R. A. Mercer, A. J. Feustel, and J. A. G. Alexander (1996). Automatic time-domain calculation of source parameters for the analysis of induced seismicity, *Bull. Seismol. Soc. Am.* **86,** no. 5, 1627–1633.

Walker, D. A., C. S. McCreery, and G. H. Sutton (1983). Spectral characteristics of high-frequency PN, SN phases in the western Pacific, *J. Geophys. Res.* **88,** no. B5, 4289–4298.

Watts, A. B., and U. S. ten Brink (1989). Crustal structure, flexure, and subsidence history of the Hawaiian Islands, *J. Geophys. Res.* **94,** no. B8, 10,473–10,500.

Wolfe, C. J., S. C. Solomon, G. Laske, J. A. Collins, R. S. Detrick, J. A. Orcutt, D. Bercovici, and E. H. Hauri (2011). Mantle *P*-wave velocity structure beneath the Hawaiian hotspot, *Earth Planet. Sci. Lett.* **303,** nos. 3/4, 267–280.

Wu, R. S., and K. Aki (1985). Elastic wave scattering by a random medium and the small-scale inhomogeneities in the lithosphere, *J. Geophys. Res.* **90,** no. B12, 10,261–10,273.

Zhang, J., P. Gerstoft, P. M. Shearer, H. Yao, J. E. Vidale, H. Houston, and A. Ghosh (2011). Cascadia tremor spectra: Low corner frequencies and earthquake-like high-frequency falloff, *Geochem. Geophys. Geosys.* **12,** Q10007, doi: 10.1029/2011GC003759.

Zollo, A., A. Orefice, and V. Convertito (2014). Source parameter scaling and radiation efficiency of microearthquakes along the Irpinia fault zone in southern Apennines, Italy, *J. Geophys. Res.* **119,** 3256–3275, doi: 10.1002/2013JB010116.

Hawai'i Institute of Geophysics and Planetology
University of Hawai'i at Mānoa
POST 602
1680 East-West Road
Honolulu, Hawaii 96822
rgb@hawaii.edu

Manuscript received 31 March 2018;
Published Online 4 September 2018